

# Rapid Optical Variations Correlated with X-rays in the 2015 Second Outburst of V404 Cygni (GS 2023+338)

Mariko Kimura,<sup>1</sup> <sup>★</sup> Taichi Kato,<sup>1</sup> Keisuke Isogai,<sup>1</sup> Hyungsuk Tak,<sup>2</sup> Megumi Shidatsu,<sup>3</sup> Hiroshi Itoh,<sup>4</sup> Tamás Tordai,<sup>5</sup> Kiyoshi Kasai,<sup>6</sup> William Goff,<sup>7</sup> Seiichiro Kiyota,<sup>8</sup> Roger D. Pickard,<sup>9,10</sup> Katsura Matsumoto,<sup>11</sup> Naoto Kojiguchi,<sup>11</sup> Yuki Sugiura,<sup>11</sup> Eiji Yamada,<sup>11</sup> Taiki Tatsumi,<sup>11</sup> Atsushi Miyashita,<sup>12</sup> Pavol A. Dubovsky,<sup>13</sup> Igor Kudzej,<sup>13</sup> Enrique de Miguel,<sup>14,15</sup> William L. Stein,<sup>16</sup> Yutaka Maeda,<sup>17</sup> Elena P. Pavlenko,<sup>18</sup> Aleksei A. Sosnovskij,<sup>18</sup> Julia V. Babina,<sup>18</sup> Lewis M. Cook<sup>19</sup> and Daisaku Nogami<sup>1</sup>

<sup>1</sup>Department of Astronomy, Graduate School of Science, Kyoto University, Oiwakecho, Kitashirakawa, Sakyo-ku, Kyoto 606-8502, Japan

<sup>2</sup>Statistical and Applied Mathematical Sciences Institute, Durham, NC, USA

<sup>3</sup>MAXI team, RIKEN, 2-1 Hirosawa, Wako, Saitama 351-0198, Japan

<sup>4</sup>Variable Star Observers League in Japan (VSOLJ), 1001-105 Nishiterakata, Hachioji, Tokyo 192-0153, Japan

<sup>5</sup>Polaris Observatory, Hungarian Astronomical Association, Laborc utca 2/c, 1037 Budapest, Hungary

<sup>6</sup>Baselstrasse 133D, CH-4132 Muttenz, Switzerland

<sup>7</sup>American Association of Variable Star Observers (AAVSO), 13508 Monitor Lane, Sutter Creek, California 95685, USA

<sup>8</sup>Variable Star Observers League in Japan (VSOLJ), 7-1 Kitahatsutomi, Kamagaya, Chiba 273-0126, Japan

<sup>9</sup>The British Astronomical Association, Variable Star Section (BAA VSS), Burlington House, Piccadilly, London W1J 0DU, UK

<sup>10</sup>3 The Birches, Shobdon, Leominster, Herefordshire HR6 9NG, UK

<sup>11</sup>Osaka Kyoiku University, 4-698-1 Asahigaoka, Kashiwara, Osaka 582-8582, Japan

<sup>12</sup>Seikei Meteorological Observatory, Seikei High School, Kichijoji-kitamachi 3-10-13, Musashino, Tokyo 180-8633, Japan

<sup>13</sup>Vihorlat Observatory, Mierova 4, Hurnenne, Slovakia

<sup>14</sup>Departamento de Física Aplicada, Facultad de Ciencias Experimentales, Universidad de Huelva, 21071 Huelva, Spain

<sup>15</sup>Center for Backyard Astrophysics, Observatorio del CIECEM, Parque Dunar, Matalascañas, 21760 Almonte, Huelva, Spain

<sup>16</sup>6025 Calle Paraíso, Las Cruces, New Mexico 88012, USA

<sup>17</sup>12-2 Kaminishiyama-machi, Nagasaki, Nagasaki 850-0006, Japan

<sup>18</sup>Crimean Astrophysical Observatory, 298409 Nauchny, Crimea

<sup>19</sup>Center for Backyard Astrophysics (Concord), 1730 Helix Court, Concord, California 94518, USA

Accepted XXX. Received YYY; in original form ZZZ

## ABSTRACT

We present optical multi-colour photometry of V404 Cyg during the outburst from December, 2015 to January, 2016 together with the simultaneous X-ray data. This outburst occurred less than 6 months after the previous outburst in June–July, 2015. These two outbursts in 2015 were of a slow rise and rapid decay-type and showed large-amplitude ( $\sim 2$  mag) and short-term ( $\sim 10$  min–3 hours) optical variations even at low luminosity ( $0.01$ – $0.1L_{\text{Edd}}$ ). We found correlated optical and X-ray variations in two  $\sim 1$  hour time intervals and obtained a Bayesian estimate of an X-ray delay against the optical emission, which is  $\sim 30$ – $50$  s, during those two intervals. In addition, the relationship between the optical and X-ray luminosity was  $L_{\text{opt}} \propto L_{\text{X}}^{0.25\text{--}0.29}$  at that time. These features cannot be easily explained by the conventional picture of transient black-hole binaries, such as canonical disc reprocessing and synchrotron emission related to a jet. We suggest that the disc was truncated during those intervals and that the X-ray delays represent the required time for propagation of mass accretion flow to the inner optically-thin region with a speed comparable to the free-fall velocity.

**Key words:** accretion, accretion disc – black holes physics – binaries: general – X-ray: stars – stars: individual (V404 Cygni)

## 1 INTRODUCTION

Transient low-mass X-ray binaries (LMXBs) are composed of a central neutron star or black hole and a low-mass companion star with an accretion disc around the central object. They show sporadic outbursts lasting for dozens of days up to several years in mainly X-rays and other wavelengths (Tanaka & Shibasaki 1996). The outbursts are considered to be caused by thermal-viscous instability over the accretion discs (see chapter 5 of Kato et al. 2008; Lasota 2001; Dubus et al. 2001). During their outbursts, reprocessing of X-ray irradiation in the outer cool discs has long been thought to dominate optical flux (Shakura & Sunyaev 1973). On the other hand, some LMXBs show rapid optical variations having timescales between milliseconds and minutes in quiescence and the low/hard state (e.g., Hynes et al. 2004; Motch et al. 1982; Uemura et al. 2002). The origin of optical emission of these short-term variations is still unclear.

V404 Cyg is a member of these transient LMXBs. This system hosts a  $9M_{\odot}$  black hole (Khargharia et al. 2010) and a  $0.7M_{\odot}$  companion star of spectral type K0( $\pm 1$ ) III-V (Shahbaz et al. 1994; Wagner et al. 1992; Casares et al. 1993; Hynes et al. 2009). It is located at a distance of 2.4 kpc (Miller-Jones et al. 2009). It was originally discovered as a nova in 1938 and its 1989 outburst was detected as an X-ray transient by the *GINGA* satellite (Makino 1989). At that time, the optical counterpart was subsequently identified with the 1938 nova (Wagner et al. 1989). During the 1989 outburst, short-term X-ray variability was observed (e.g., Źycki et al. 1999). On June 15th in 2015, it underwent a short outburst after 26 years of quiescence (Barthelmy et al. 2015a) and showed large flares in radio (Mooley et al. 2015; Tetarenko et al. 2015), infrared (Tanaka et al. 2016), optical (Rodriguez et al. 2015; Martí et al. 2016; Kimura et al. 2016; Gandhi et al. 2016), X-ray (King et al. 2015; Natalucci et al. 2015; Negoro et al. 2015; Segreto et al. 2015; Walton et al. 2017; Radhika et al. 2016; Jourdain et al. 2017; Huppenkothen et al. 2017) and gamma-ray wavelengths (Roques & Jourdain 2016; Siegert et al. 2016; Jenke et al. 2016; Loh et al. 2016; Piano et al. 2017).

This system exhibited violent optical variations with regular patterns for some intervals during the 2015 June outburst, when most of the optical flux was likely to be produced by the reprocessing of X-ray irradiation in the outer disc (Kimura et al. 2016). A lack of optical and near-infrared polarisation was reported by Tanaka et al. (2016) in two periods during the outburst. There was, however, evidence of a strong contribution of synchrotron emission related to jet ejections in some other epochs (Rodriguez et al. 2015; Martí et al. 2016; Shahbaz et al. 2016; Lipunov et al. 2016; Bernardini et al. 2016b). Gandhi et al. (2016) found sub-second optical flaring events and proposed that not only X-ray reprocessing but also non-thermal emission contributed to them. Thus the origin of optical emission in the outburst is still under debate.

At 05:19:52 UT on December 23rd, 2015, the *Swift* Burst Alert Telescope (BAT) initially detected that the X-ray flux increased above the detection limit (Barthelmy et al. 2015b). Just after the BAT detection, MASTER-Amur began observing this object on December 23.385 UT in optical wavelengths (Lipunov et al. 2015). Muñoz-Darias et al.

(2017) reported evidence of a strong wind with their optical spectroscopy and the multi-wavelength variability, which were very similar to those in the June outburst. In this paper, we report on our optical photometry of the December outburst in V404 Cyg and study their correlation with the simultaneous X-ray data of *INTEGRAL* Imager on Board the Integral Satellite (IBIS)/CdTe array (ISGRI) monitoring.

## 2 OBSERVATION AND ANALYSIS

### 2.1 Optical Observations

Time-resolved CCD photometry was carried out by the Variable Star Network (VSNET) collaboration team (Kato et al. 2004) at 17 sites (Table S1) in the 2015 December outburst in V404 Cyg. Table S2 shows the log of our photometric observations in the  $V$ ,  $R_C$  and  $I_C$  bands and with a clear filter. The exposure times were 15–540 s. We also used the data downloaded from the American Association of Variable Star Observers (AAVSO) archive<sup>1</sup>. All of the observation times were converted to barycentric Julian date (BJD). The comparison stars are listed in Table S3. The constancy of the comparison stars was checked by nearby stars in the same images. The data reduction and the calibration of the comparison stars were performed by each observer. The magnitude of each comparison star was measured by A. Henden from the AAVSO Variable Star Database<sup>2</sup>. The tables are displayed in the supplements to this paper.

### 2.2 X-ray Analysis

We extracted X-ray light curves with time bin sizes of 1 s and 5 s in the 25–60 keV energy band to use them for timing analyses (Sec. 3.2 and 3.3) from the archived data of the *INTEGRAL* IBIS/ISGRI monitoring set. We employed the latest version of the standard data analysis software `Off line Scientific Analysis (OSA)` v.10.2<sup>3</sup> for pipeline processing. The publicly available pointing observations between MJD 57387.65–57387.80 are composed of 4 science windows (SCWs). Each of the SCWs has a typical good time of  $\sim 3$  ks in duration. An image in the 25–60 keV energy band was generated from IBIS-ISGRI data by using an input catalogue, `gnrl_refr_cat_0039.fits`. Background maps provided by the ISGRI team were used for background correction. We put `gnrl_refr_cat_0039.fits` [ISGRI\_FLAG2==5 && ISGRI\_FLUX\_1>100] (the default parameter) in the parameter “brSrcDOL” in the IBIS Graphical User Interface. The spectra and 1-s and 5-s binned light curves were extracted with the tool `ii_light` and a catalogue composed of the strong sources in the field of view (FOV); AX J1949.8+2534, Cygnus X-1, Cygnus X-3 and Ginga 2023+338 (V404 Cyg). We derived the X-ray light curves in flux scales using a conversion parameter of 1 [count s<sup>-1</sup>] to be  $5.632 \times 10^{-11}$  [ergs cm<sup>-2</sup> s<sup>-1</sup>] with the HEAsoft package assuming a Crab-like spectrum. Moreover, we obtained lists of photons in the

<sup>1</sup> <<http://www.aavso.org/data/download/>>

<sup>2</sup> <<http://www.aavso.org/vsp>>

<sup>3</sup> <<http://www.isdc.unige.ch/integral/analysis#Software>>

SCWs with the tool `ii_pif` to use them for power spectral analyses (Sec. 3.3). All of the observation times were converted to BJD.

To estimate the bolometric correction factor  $L_{\text{bol}}/L_{25-60\text{keV}}$ <sup>4</sup>, we analysed multi-wavelength spectral energy distributions (SEDs) in two intervals (during BJD 2457382.85–2457382.86 and BJD 2457386.58–2457386.60), when the source was fully simultaneously observed in X-rays (*Swift*/X-ray Telescope (XRT) data, obsID: 00031403127 and 00031403131, respectively) and optical bands, assuming that they can be reproduced with the same irradiated disc model employed by [Kimura et al. \(2016\)](#) for the 2015 June–July outburst. The estimated bolometric correction factors in these two intervals were 9.1 (ID 00031403127) and 10 (ID 00031403131), respectively. These values were almost the same as that of the estimated correction factor (9.97) in the previous outburst (see ED Fig. 6(a) in [Kimura et al. 2016](#)). We then adopted the same correction factor, 9.97, to estimate  $L_{\text{bol}}$  from the *INTEGRAL* IBIS/ISGRI X-ray 25–60 keV light curves in the 2015 December outburst.

### 3 RESULTS

#### 3.1 Rapid Optical Variations

We detected large-amplitude and short-term optical variations with amplitudes ranging from 0.4 to 2.5 mag on timescales of  $\sim$ 10 min–3 hours during the 2015 December outburst in V404 Cyg. The bolometric luminosity derived from the X-ray flux with the correction factor (see Sec. 2.2) was low. The overall optical light curves of the outburst in the  $I_{\text{C}}$ ,  $R_{\text{C}}$ ,  $V$  and no-filter bands, and the X-ray 25–60 keV light curves of *INTEGRAL* IBIS/ISGRI monitoring with time bin size of 64 s downloaded from the archive data<sup>5</sup> ([Kuulkers et al. 2016](#)) are displayed in Figure 1.<sup>6</sup> Hereafter, we choose BJD 2457380 as the time reference and report the time from that day. Sudden dips in brightness were detected for several time intervals (during the day 4.18–4.31 for example). The variations with amplitudes of  $\gtrsim$ 2 mag were observed only when the nightly average magnitude was brighter than  $\sim$ 14.2 mag in the  $I_{\text{C}}$  band, in the middle term of the outburst. The maximum magnitude in the brightest interval during the December outburst (the day 8.24–8.34) was 11.3 mag in the  $I_{\text{C}}$  band and the maximum bolometric luminosity in that interval was  $4.37 \times 10^{-1} L_{\text{Edd}}$ . The average brightness gradually increased during the day 0–7.5, was constant during the day 7.5–8.8 and rapidly decreased during the day 8.8–11.3. A small rebrightening was observed soon after the rapid decay (see the  $I_{\text{C}}$ -band light curves in Figure 1).

#### 3.2 Optical and X-ray Correlation

We found the simultaneous X-ray data with our optical data for two intervals (1) during the day 8.18–8.22 and (2) during the day 8.246–8.292 where stochastic variations were ob-

<sup>4</sup> Here,  $L_{\text{bol}}$  is the bolometric luminosity.

<sup>5</sup> <http://www.isdc.unige.ch/integral/analysis/#QLAsources>

<sup>6</sup> The X-ray light curves are adaptively rebinned to achieve signal-to-noise ratio (S/N)  $> 8$  by the *INTEGRAL* team.

served (see the grey shadings in Figure 1).<sup>7</sup> The enlarged view of the intervals is displayed in Figure 2. To examine the correlations between the optical and X-ray luminosity, we performed Spearman’s rank tests on them in logarithmic scales and power law regression assuming that they follow  $y = ax^b$ . Here,  $x$  and  $y$  denote the X-ray and optical ( $V$  or  $I_{\text{C}}$  band) luminosity in linear scales, respectively. In these analyses, the completely simultaneous X-ray light curves to the optical ones were obtained by binning the *INTEGRAL* IBIS/ISGRI 25–60 keV light curves having 1-s time bin size<sup>8</sup> with the exposure times of the optical observations (30 s for interval (1) and 50 s or 60 s for interval (2)) and calculating weighted averaged flux in each bin. The optical data are corrected for interstellar extinction/absorption by assuming  $A_V = 4$  ([Casares et al. 1993; Cardelli et al. 1989](#)). The results are summarised in Table 1. Both analyses have confirmed the correlated variations. Optical vs. X-ray luminosity during the two time intervals is displayed in Figure 3 with the regression equations.

**Table 1.** Results of Spearman’s rank tests and power law regression for the model of form,  $y = ax^b$ , in time intervals (1) on the day 8.18–8.22 and (2) on the day 8.246–8.292.

Intervals	$a^*$	$b^*$	$\rho^{\dagger}$	$p\text{-value}^{\ddagger}$
(1)	$10^{(25.9 \pm 2.076)}$	$0.255 (\pm 0.0568)$	0.60	$4.546 \times 10^{-6}$
(2)	$10^{(24.3 \pm 1.431)}$	$0.290 (\pm 0.0388)$	0.71	$4.573 \times 10^{-11}$

<sup>\*</sup>The values of degree of freedom (d.o.f) of the regression in time intervals (1) and (2) are 49 and 61, respectively. As a result of  $t$ -tests of the regression coefficients,  $t$ -values of  $a$  and  $b$  were 12.495 ( $p < 2 \times 10^{-16}$ ) and 4.487 ( $p = 4.37 \times 10^{-5}$ ) for interval (1) and 16.988 ( $p < 2 \times 10^{-16}$ ) and 7.472 ( $p = 3.57 \times 10^{-10}$ ) for interval (2), respectively. These tests prove the estimated values of  $a$  and  $b$  to be statistically significant at the 1% level. In addition, the values of  $F$ -tests were 20.84 ( $p = 4.371 \times 10^{-5}$ ) for interval (1) and 55.83 ( $p = 3.567 \times 10^{-10}$ ) for interval (2), respectively, and hence, the assumption that  $a = b = 0$  is abandoned.

<sup>†</sup>Spearman’s correlation coefficients.

<sup>‡</sup>Null hypothesis probability of Spearman’s correlation test. The null hypothesis is abandoned because the probability values are less than 0.01.

#### 3.3 Bayesian Time Delay Analysis

We estimated time delays between our optical light curves and the *INTEGRAL* IBIS/ISGRI X-ray light curves with time bin size of 5 s in the 25–60 keV energy band for interval (1) on the day 8.18–8.22 and interval (2) on the day 8.246–8.292 using a Bayesian method that was originally proposed to estimate time delays between gravitation-

<sup>7</sup> Although some of *INTEGRAL* ToO observations were performed during some other intervals including the periods in which high-amplitude optical variations were observed (e.g., the day 6.16–6.32, the day 7.16–7.35 and the day 8.84–8.96), the luminosity was very low at that time and it was difficult to judge whether the optical and X-ray variability was correlated or not in those intervals due to the low S/N of the X-ray data.

<sup>8</sup> The 1-s binned X-ray light curves were derived with the tool `ii_light` described in Sec. 2.2.

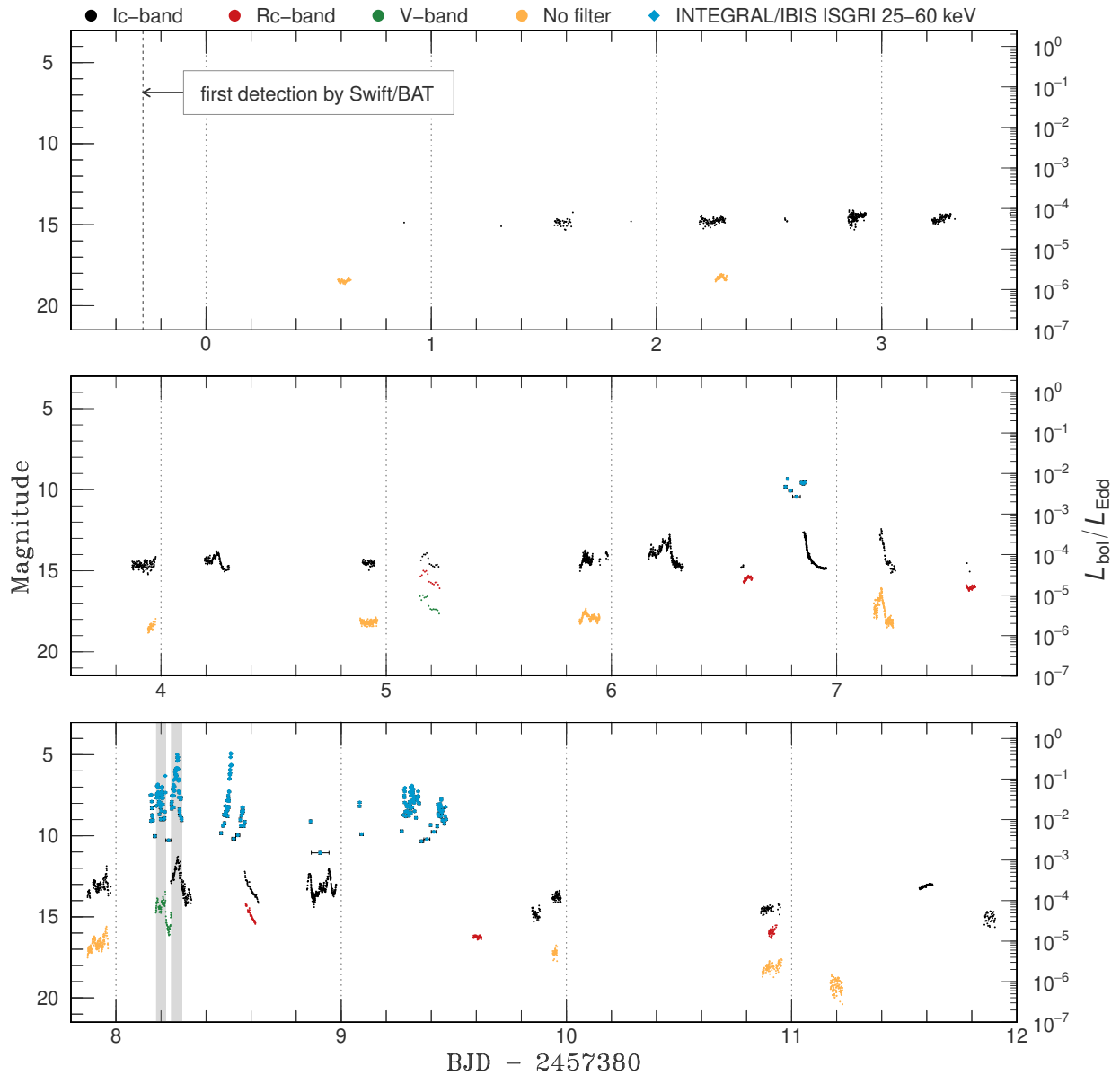


**Figure 1.** Overall light curves in the optical  $I_C$ ,  $R_C$ ,  $V$  bands and with no filter and in the X-ray 25–60 keV energy band of *INTEGRAL* IBIS/ISGRI monitoring during the 2015 December outburst in V404 Cyg. For clarity, the plotted magnitude for the unfiltered data is fainter by 2 mag than measured. The horizontal axis represents days from BJD 2457380. Here,  $L_{\text{Edd}}$  is equal to  $1.35 \times 10^{39}$  [erg/s]. For visibility, only data points having horizontal error bars less than 1 hour are plotted. The grey shadings represent the overlapped optical and X-ray observational periods.

ally lensed stochastic light curves (Tak et al. 2016a).<sup>9</sup> This method assumes that the irregularly sampled light curves are generated by a latent continuous-time damped random walk (DRW) process (Kelly et al. 2009) and that one of the latent light curves is a shifted version of the other by the time lag in the horizontal axis and by the magnitude offset

in the vertical axis (Pelt et al. 1994). The model also adopts heteroskedastic Gaussian measurement errors.

The DRW process is a stochastic process to describe a random walk with a tendency to move back towards a central location. This process is known to be appropriate for modelling accretion-type light variation such as the variability observed in active galactic nuclei (AGNs) because of its power-law type power spectral density (Kelly et al. 2009; Kozłowski et al. 2010; MacLeod et al. 2010). This process is also suitable for modelling another accretion-type

<sup>9</sup> The 5-s binned X-ray light curves were derived with the tool `ii_light` described in Sec. 2.2.

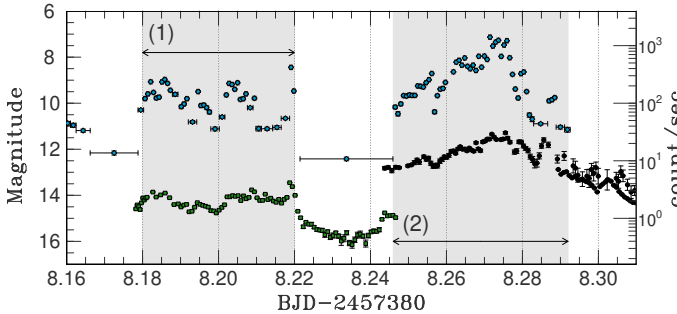


**Figure 2.** Simultaneous optical and X-ray light curves during (1) the day 8.18–8.22 and (2) the day 8.246–8.292. Each of the intervals is  $\sim 1$  hour long. The blue rhombuses, green squares and black circles represent the X-ray 25–60 keV, optical V-band and optical I<sub>c</sub>-band light curves. The optical flares are broader than the X-ray ones.

light variation in a black-hole binary. This is because the power spectral densities (PSDs) of the X-ray light variations in V404 Cyg in the SCWs (162800020010, 162800030010, 162800040010 and 162800050010) including intervals (1) and (2) are well expressed by a power-law ( $P \propto f^{-\Gamma}$ ) with an index  $\Gamma$  of  $1.6 \pm 0.1$ ,  $1.5 \pm 0.1$ ,  $1.6 \pm 0.1$  and  $1.0 \pm 0.2$ , respectively (see also Figure S1 in the supplements to this paper).<sup>10</sup>

Our data, however, do not completely meet the second model assumption (i.e., one of the latent light curves is a parallel-shifted version of the other). This is because our optical light curves have smaller amplitudes than the X-ray ones and the origin of the optical light curves may be different from that of the X-ray ones unlike gravitationally lensed light curves as originally applied in Tak et al. (2016a). Thus we scaled the X-ray light curve to the optical one using the results of the power law regression (see Sec. 3.2 and Table 1) to meet the assumption before implementing the Bayesian method; we treated the scale change in the X-ray light curve as a known constant. The data sets for our analyses are displayed in Figure 4. X-ray emission seems to be delayed to the optical emission when we focus on the sharp peaks with small measurement errors (e.g., around the day 8.209 in the upper panel and around the day 8.279 in the lower panel). The following time lag estimations enable us to investigate the delay quantitatively.

We used an R package, `timedelay`, which we made available to the public at CRAN<sup>11</sup>, to implement the Bayesian model via a Markov chain Monte Carlo (MCMC) method; see Appendix A for details of the model, implementation, and model checking. Figure 5 exhibits the histogram of 300,000 posterior samples of the time lag between the optical and X-ray light curves for interval (1) on the left panel and that for interval (2) on the right panel. The estimation results are summarised in Table 2; the posterior median of the time delay for interval (1) was  $-45.3_{-1.1}^{+0.3}$  s and that for interval (2) was  $-33.1_{-0.2}^{+0.3}$  s, i.e., the X-ray variations were

<sup>10</sup> We employed powerspec software in the FTOOLS Xronos package from the lists of photons. The values of “dtnt” and “rebin” parameters were 1 s and -1.8, respectively. The Nyquist frequency of these observations was 0.5 Hz.

<sup>11</sup> <https://cran.r-project.org/package=timedelay>

delayed to the optical variations by  $45.3_{-1.1}^{+0.3}$  s for interval (1) and  $33.1_{-0.2}^{+0.3}$  s for interval (2). The Gelman-Rubin convergence diagnostic statistics (Gelman & Rubin 1992) were 1.0004 and 1.0009 in intervals (1) and (2), respectively, close enough to unity. To check the consistency between different estimation methods, we compared our estimates with the results of a locally normalized discrete correlation function (LNDCF; Lehar et al. 1992). The LNDCF estimates averaged with time bin size equal to 25.92 s showed  $-35_{-13}^{+13}$  s time lags in both intervals (1) and (2) (see also Figure S2 in the supplements to this paper). Both Bayesian and LNDCF methods result in consistent estimates, considering the large uncertainties of the LNDCF estimates.

**Table 2.** Bayesian estimates of the time delays for interval (1) during the day 8.18–8.22 and interval (2) during the day 8.246–8.292. The 68% interval indicates the quantile-based interval and the 68% HPD interval represents the highest posterior density interval.

Intervals	Median*	68% Interval	68% HPD Interval
(1)	-45.4 s	(-46.5 s, -45.1 s)	(-45.6 s, -45.0 s)
(2)	-33.1 s	(-33.3 s, -32.8 s)	(-33.4 s, -32.9 s)

\*We report posterior medians because posterior means are not reliable indicators for the centre of a multi-modal distribution. The posterior mode and median of time delays are identical up to three decimal places for interval (1). For interval (2), the posterior mode is -33.2 s.

## 4 DISCUSSION

### 4.1 Similarities between the Two Outbursts in 2015

Large-amplitude and short-term optical variations at low luminosity, which have good correlations with simultaneous X-ray variability, were observed during the two outbursts in 2015 in V404 Cyg (see also Kimura et al. 2016). This behaviour seems to be a common feature in every outburst of this system. Actually, violent optical variations with amplitudes of  $\sim 1$  mag on timescales of days or minutes were observed also in the late stage of the 1989 outburst (Wagner et al. 1991). The amplitudes and timescales of these optical variations and the occasional sudden dips in brightness during the December outburst were similar to those during the June outburst.

The overall trend of our optical light curves (a slow rise and rapid decay) in the December outburst was also similar to that in the June/July outburst as Muñoz-Darias et al. (2017) already pointed out. This trend is different from the most common type of outburst in transient LMXBs (Chen et al. 1997). The slow rise could be the result of an inside-out outburst which is considered to arise more frequently than an outside-in outburst in these objects (Lasota 2001, for a review). This possibility has already been suggested during the June outburst by estimating the disc radius at which an optical precursor was ignited (Bernardini et al. 2016a).

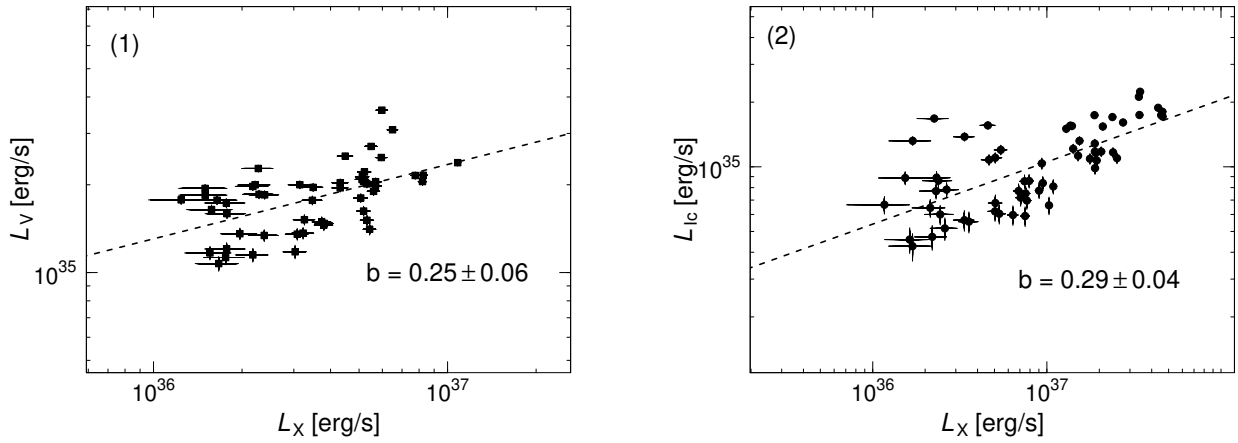


**Figure 3.** Optical and X-ray correlations during interval (1) on the day 8.18–8.22 (the left panel) and interval (2) on the day 8.246–8.292 (the right panel). The filled squares and circles represent the optical  $V$ -band and  $I_C$ -band luminosity. The horizontal axes exhibit X-ray luminosity in the 25–60 keV energy band. The dashed lines represent the estimated power law regression formulae for the relations between the optical and X-ray luminosity. The values of the power law index ( $b$ ) are also reported.

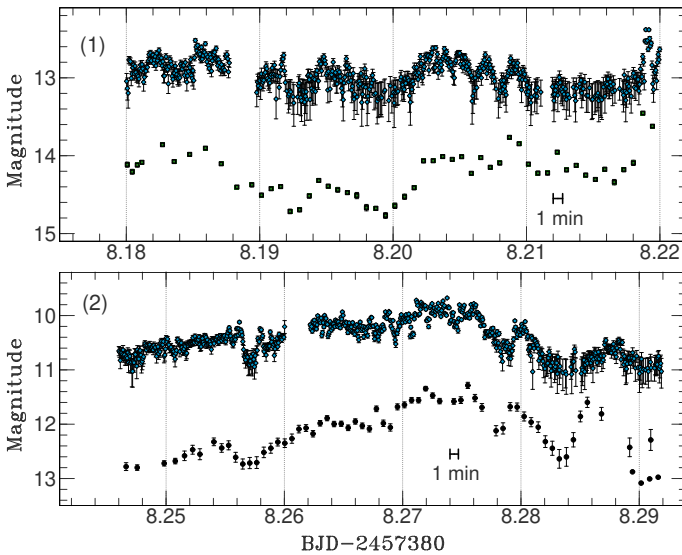


**Figure 4.** X-ray and optical data sets used for the time delay estimates in interval (1) during the day 8.18–8.22 and interval (2) during the day 8.246–8.292. The X-ray light curves are rescaled by using the results of power law regression described in Sec. 3.2. The rhombuses, squares and circles represent the X-ray light curves in the 25–60 keV energy band with time bin size of 5 s after scaling, the optical  $V$ -band light curves and the optical  $I_C$ -band light curves. For visibility, the X-ray magnitudes are offset by 7.7 for interval (1) and 4.7 for interval (2), respectively.

#### 4.2 Differences in the Short-term Variability between the Two Outbursts in 2015

Although the morphology of violent and rapid optical variations during the June and December outbursts resemble each other, the nature of these variations during the December outburst seems to be different from those during the June outburst. This is because we found X-ray variations lagging

optical ones by  $\sim$ 30–50 s for the two intervals during the December outburst (Sec. 3.3), which had not been detected during the June outburst. We consider whether two commonly known mechanisms of optical emission in X-ray binaries could explain the X-ray delays. They were expected to have been dominant at least some time intervals during the June outburst. The first one is the reprocessing of X-ray irradiation from the inner disc (e.g., [van Paradijs & McClintock 1994](#)) and the second one is cyclo-synchrotron emission from magnetic flares, which would be related to a jet (e.g., [Merloni et al. 2000](#); [Markoff et al. 2001](#)). X-ray reprocessing will produce optical delays against X-rays on timescales of tens of seconds (e.g., [Hynes et al. 1998](#)). On the other hand, cyclo-synchrotron radiation will induce very short time lags within 1 s between optical and X-ray variations, which are not consistent with the lags caused by X-ray reprocessing (e.g., [Kanbach et al. 2001](#)).<sup>12</sup> We, therefore, conclude that these processes would fail to explain the observed X-ray delays in the December outburst. Even if we observed the expanding jet ejecta, the expected time lag was a  $\gtrsim$ 10 min optical delay ([van der Laan 1966](#); [Mirabel et al. 1998](#)) as discussed also in the June outburst ([Rodriguez et al. 2015](#); [Martí et al. 2016](#)). It is quite different from the X-ray delays that we estimated.

There are some other models including synchrotron radiation, which have been developed to explain recently detected anti-correlated cross-correlation function (CCF) signals with X-ray emission lagging optical one by a few seconds and narrower optical auto-correlation functions (ACFs) to X-ray ones in several LMXBs (e.g., [Gandhi et al. 2008](#); [Durant et al. 2008](#); [Malzac et al. 2004](#); [Veledina et al. 2011](#)). The timescales of the X-ray delays detected in this study,

<sup>12</sup> There may be a possibility that the very short time lag is not found because the observational data used in this work do not allow investigating millisecond-scale timing properties.

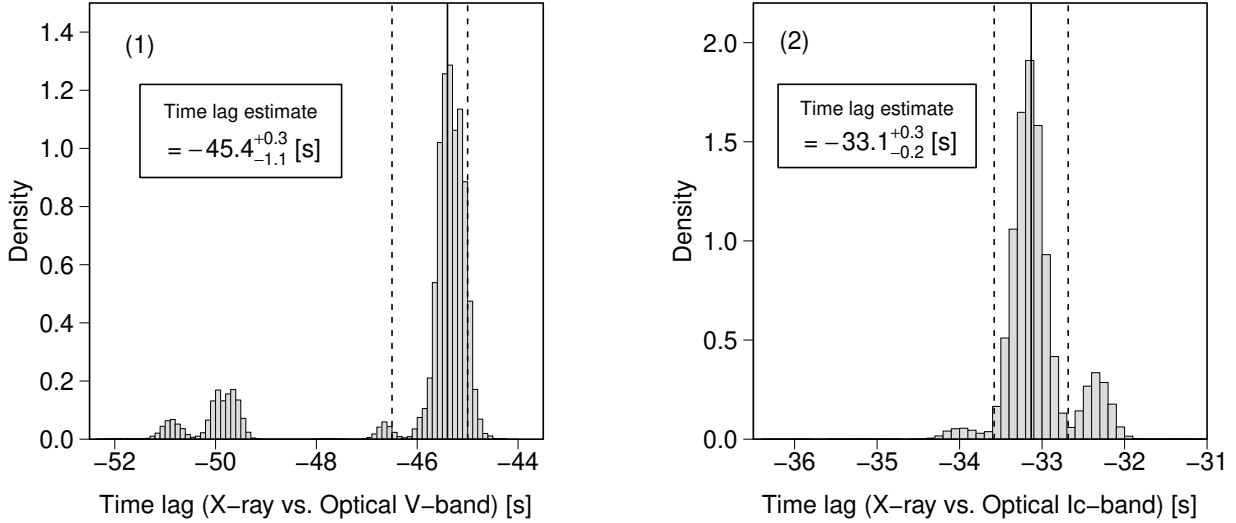


**Figure 5.** Posterior distributions of the time delays of the optical variations against the X-ray ones for interval (1) on the day 8.18-8.22 (the left panel) and interval (2) on the day 8.246-8.292 (the right panel). The solid line indicates the posterior median of the time lag and the dashed lines represent the 68% quantile-based interval. The time lag estimate shown in each figure is the posterior median with 68% quantile-based interval. There are invisibly small modes near  $-30.5$  s and  $-25.8$  s in the posterior distribution for interval (1) and near  $-48.1$  s in that for interval (2), but we displayed only major modes.

however, are inconsistent with the odd timing properties expected by these models as well as the smoother optical flares to the X-ray ones and the positive peaks at negative optical time lags in the DCFs (see also Figures 2 and S2).

There is some evidence to support that the effect of X-ray reprocessing and/or cyclo-synchrotron emission was weak. First, the estimated relation between the optical and X-ray luminosity in Sec. 3.2 was  $L_{\text{opt}} \propto L_X^{0.25-0.29}$  and this value disagrees with both that expected by standard disc reprocessing ( $L_V \propto L_X^{0.5}$ , van Paradijs & McClintock 1994) and that predicted by jet ejections plus X-ray irradiation ( $L_{\text{opt}} \propto L_X^{0.5-0.7}$ , Russell et al. 2006). Second, the optical/X-ray flux ratios in the December outburst ( $\sim 0.05$  in the  $V$  band and  $\sim 0.01$  in the  $I_C$  band) were smaller by a factor of 2–5 than those in the June outburst when X-ray reprocessing considerably dominated the optical flux. This would indicate that the effect of reprocessing was weaker in the December outburst than that in the June outburst. We suggest the reason is that the outer disc would be depleted due to ionisation during the June outburst and/or the strong outflow discussed in Muñoz-Darias et al. (2016). On the other hand, in the June outburst, the outer disc is thought to have been optically thick (Kimura et al. 2016).

#### 4.3 Time Delay Caused by Propagation of Mass Accretion Flow in the Inner Disc

We propose an interpretation that short-term variations of the mass-accretion rate in the outer disc (whose origin is still unknown) propagate to the inner disc via optical fluctuations which will thereby prompt X-ray fluctuations. This then replaces the mechanisms discussed in the previous subsection as a possible origin of the delays. If the standard thin disc extends close to the central black hole, it will take longer for the observed delays to propagate in an accretion flow from the optical emission region to the X-ray

emission region. This is because the speed of a propagating heating wave is proportional to the speed of sound ( $c_s$ ) in the standard disc (i.e.,  $v_f \sim \alpha c_s$ ; Meyer 1984). Here,  $\alpha$  represents the viscous parameter. Thus we consider the condition that the disc is composed of an optically-thin flow as an advection-dominated accretion flow (ADAF) and a truncated geometrically-thin standard disc. This picture was considered during the 2002 outburst in V4641 Sgr, another black-hole transient LMXB, when a 7-min delay of the X-ray variations against the optical ones was detected at the fading stage (Uemura et al. 2004).

We assume that the thin standard disc extended to the transition radius ( $R_{\text{tr}}$ ) and that there was the ADAF on the inside of the radius (e.g., Hameury et al. 1997). In the ADAF, the matter moves to the central object with a speed comparable to the free-fall velocity ( $v_{\text{ff}}$ ) ( $v_f \sim \alpha v_{\text{ff}}$ ; Narayan & Yi 1995). If the optical fluctuations, which were triggered at a region close to the truncation radius, propagated to the central black hole via the accretion of mass flow on the free-fall timescale in the ADAF, the transition radius is estimated to be  $\sim 2.5-4.0 \times 10^8$  [cm] by using the above approximation for  $\alpha = 0.01$  (Sano et al. 1998; Machida & Matsumoto 2003) and our estimates of X-ray delays. The estimated value of  $R_{\text{tr}}$  corresponds to  $\sim 100-150 r_s$ . Here,  $r_s (= 2GM/c^2)$  represents the Schwarzschild radius for a  $9M_\odot$  black hole. The estimated value is close to that of the inner disc radius derived through the SED analyses in the June outburst (see Sec. 8 of Methods in Kimura et al. 2016). The region at the radius is, however, too hot to emit thermal optical photons predominantly; hence the picture may be problematic. It is likely that the optical emission was non-thermal as discussed in e.g., Uemura et al. (2002). In addition, the smaller amplitude of the optical variations can be explained by the presence of the optical continuum emission from the outer disc.

#### 4.4 Testing Possibilities of the Origin of X-ray Delays

An optically-thin flow like an ADAF inside a truncated standard disc has been widely proposed as a possible scenario for the low/hard state in black-hole X-ray binaries, although the interpretation remains under discussion (Remillard & McClintock 2006; Done et al. 2007; Belloni et al. 2011, for a review). The average value of the bolometric luminosity during intervals (1) and (2),  $0.03\text{--}0.1L_{\text{Edd}}$ , is consistent with the low/hard state (Done & Gierliński 2003; Dunn et al. 2010), the existing theory (Yuan et al. 2007) and the 3D magnetohydrodynamics (MHD) simulations (Machida et al. 2006; Oda et al. 2007). The spectral state was also reported to be the low/hard state during the day 8.15–10.32 (Motta et al. 2016); however, a detailed spectral analysis would be useful to test our interpretation since the peculiar X-ray spectral behaviour similar to that of an obscured AGN was found for some time intervals during the June outburst by Sanchez-Fernandez et al. (2017) and Motta et al. (2017). They suggested, on the basis of the spectral behaviour, that optically thick outflowing material would obscure substantial X-rays from the central part of V404 Cyg and that the intrinsic luminosity was close to the Eddington luminosity. This situation implies the existence of a slim disc; however, it would be difficult for short-term variability and time delays to coexist in this circumstance.<sup>13</sup> Additionally, a slim disc itself would be difficult to maintain during the December outburst since the averaged X-ray flux during this outburst was much smaller than that during the June outburst.

## 5 CONCLUSIONS

We report on the photometric observations in the outburst of V404 Cyg from December, 2015 to January, 2016. Our main findings are summarised below.

(i) The 2015 December outburst in V404 Cyg was very similar to the 2015 June–July outburst in the following two aspects. One is that violent and rapid optical variability with amplitudes of  $\sim 2$  mag on timescales of  $\sim 10$  min–3 hours was observed at low luminosity. It is likely that this kind of variation is commonly seen in the outbursts including the 1989 one in this object. The other is that the trend of the overall light curves was a slow rise and rapid decay.

(ii) We detected an X-ray delay of  $\sim 30\text{--}50$  s against the optical emission in the two intervals during the December outburst, when the large-amplitude stochastic optical variations were observed at the low average luminosity,  $\sim 0.03\text{--}0.1L_{\text{Edd}}$ . In addition, the relation between the optical and X-ray luminosity for these two intervals was  $L_{\text{opt}} \propto L_{\text{X}}^{0.25\text{--}0.29}$ . We suggest that the X-ray delay can be due to propagation of mass accretion flow in an inner optically-thin hot flow like an ADAF with a speed comparable to the free-fall velocity.

<sup>13</sup> Sporadic mass accretion is unlikely to occur due to the high accretion rate in a slim disc. A variable absorber to cause the observed variability in the June outburst was suggested by Sanchez-Fernandez et al. (2017) and Motta et al. (2017) instead, but this condition would not produce time lags between optical and X-ray emission.

## ACKNOWLEDGEMENTS

We acknowledge the variable star observations from the AAVSO International Database contributed by observers worldwide and used in this research. We also thank the *INTEGRAL* groups for making the products of the ToO data publicly available online at the *INTEGRAL* Science Data Centre. This work was financially supported by the Grant-in-Aid for JSPS Fellows for young researchers (MK) and the Grant-in-Aid “Initiative for High-Dimensional Data-Driven Science through Deepening of Sparse Modeling” from the Ministry of Education, Culture, Sports, Science and Technology (MEXT) of Japan (25120007, TK). It was also partially supported by the RFBR grant 15-02-06178. We are thankful to many amateur observers for providing a lot of data used in this research. Hyungsuk Tak acknowledges partial support from the United States National Science Foundation under Grant DMS 1127914 to the SAMSI. We give special thanks to Kaisey Mandel and David van Dyk for very helpful discussions. Yutaro Tachibana provided us with a code for calculations of LNDCFs. Roger D. Pickard gratefully acknowledges use of the Las Cumbres Observatory Global Telescope Network. We are grateful to an anonymous referee for his/her helpful comments.

## REFERENCES

Barthelmy S. D., D’Ai A., D’Avanzo P., Krimm H. A., Lien A. Y., Marshall F. E., Maselli A., Siegel M. H., 2015a, GRB Coordinates Network, 17929  
 Barthelmy S. D., Page K. L., Palmer D. M., 2015b, GRB Coordinates Network, 18716  
 Belloni T. M., Motta S. E., Muñoz-Darias T., 2011, Bulletin of the Astronomical Society of India, 39, 409  
 Bernardini F., Russell D. M., Shaw A. W., Lewis F., Charles P. A., Koljonen K. I. I., Lasota J. P., Casares J., 2016a, ApJ, 818, L5  
 Bernardini F., Russell D. M., Koljonen K. I. I., Stella L., Hynes R. I., Corbel S., 2016b, ApJ, 826, 149  
 Cardelli J. A., Clayton G. C., Mathis J. S., 1989, ApJ, 345, 245  
 Casares J., Charles P. A., Naylor T., Pavlenko E. P., 1993, MNRAS, 265, 834  
 Chen W., Shrader C. R., Livio M., 1997, ApJ, 491, 312  
 Done C., Gierliński M., 2003, MNRAS, 342, 1041  
 Done C., Gierliński M., Kubota A., 2007, A&ARv, 15, 1  
 Dubus G., Hameury J.-M., Lasota J.-P., 2001, A&A, 373, 251  
 Dunn R. J. H., Fender R. P., Körding E. G., Belloni T., Cabanac C., 2010, MNRAS, 403, 61  
 Durant M., Gandhi P., Shahbaz T., Fabian A. P., Miller J., Dhillon V. S., Marsh T. R., 2008, ApJ, 682, L45  
 Gandhi P., et al., 2008, MNRAS, 390, L29  
 Gandhi P., et al., 2016, MNRAS, 459, 554  
 Gelman A., Rubin D. B., 1992, Statistical Science., pp 457–472  
 Hameury J.-M., Lasota J.-P., McClintock J. E., Narayan R., 1997, ApJ, 489, 234  
 Huppenkothen D., et al., 2017, ApJ, 834, 90  
 Hynes R. I., O’Brien K., Horne K., Chen W., Haswell C. A., 1998, MNRAS, 299, 37P  
 Hynes R. I., et al., 2004, ApJ, 611, L125  
 Hynes R. I., Bradley C. K., Rupen M., Gallo E., Fender R. P., Casares J., Zurita C., 2009, MNRAS, 399, 2239  
 Jenke P. A., et al., 2016, ApJ, 826, 37  
 Jourdain E., Roques J.-P., Rodi J., 2017, ApJ, 834, 130  
 Kanbach G., Straubmeier C., Spruit H. C., Belloni T., 2001, Nature, 414, 180

Kato T., Uemura M., Ishioka R., Nogami D., Kunjaya C., Baba H., Yamaoka H., 2004, PASJ, 56, S1

Kato S., Fukue J., Mineshige S., 2008, Kyoto University Press (Kyoto, Japan), Black-Hole Accretion Disks — Towards a New Paradigm —

Kelly B. C., Bechtold J., Siemiginowska A., 2009, ApJ, 698, 895

Khargharia J., Froning C. S., Robinson E. L., 2010, ApJ, 716, 1105

Kimura M., et al., 2016, Nature, 529, 54

King A. L., Miller J. M., Raymond J., Reynolds M. T., Moringstar W., 2015, ApJ, 813, L37

Kozłowski S., et al., 2010, ApJ, 708, 927

Kuulkers E., amp Ferrigno C., 2016, The Astronomer's Telegram, 8512

Lasota J.-P., 2001, New Astron. Rev., 45, 449

Lehar J., Hewitt J. N., Burke B. F., Roberts D. H., 1992, ApJ, 384, 453

Lipunov V., et al., 2015, The Astronomer's Telegram, 8453

Lipunov V. M., et al., 2016, ApJ, 833, 198

Loh A., et al., 2016, MNRAS, 462, L111

MacLeod C. L., et al., 2010, ApJ, 721, 1014

Machida M., Matsumoto R., 2003, ApJ, 585, 429

Machida M., Nakamura K. E., Matsumoto R., 2006, PASJ, 10.1093/pasj/58.1.193, 58, 193

Makino F., 1989, IAU Circ., 4782

Malzac J., Merloni A., Fabian A. C., 2004, MNRAS, 351, 253

Markoff S., Falcke H., Fender R., 2001, A&A, 372, L25

Martí J., Luque-Escamilla P. L., García-Hernández M. T., 2016, A&A, 586, A58

Merloni A., Di Matteo T., Fabian A. C., 2000, MNRAS, 318, L15

Meyer F., 1984, A&A, 131, 303

Miller-Jones J. C. A., Jonker P. G., Dhawan V., Brisken W., Rupe M. P., Nelemans G., Gallo E., 2009, ApJ, 706, L230

Mirabel I. F., Dhawan V., Chaty S., Rodriguez L. F., Marti J., Robinson C. R., Swank J., Geballe T., 1998, A&A, 330, L9

Mooley K., Fender R., Anderson G., Staley T., Kuulkers E., Rumsey C., 2015, The Astronomer's Telegram, 7658

Motch C., Illovaisky S. A., Chevalier C., 1982, A&A, 109, L1

Motta S. E., Sanchez-Fernandez C., Kuulkers E., Kajava J., Bozzo E., 2016, The Astronomer's Telegram, 8500

Motta S. E., Kajava J. J. E., Sánchez-Fernández C., Giustini M., Kuulkers E., 2017, MNRAS, 468, 981

Muñoz-Darias T., et al., 2016, Nature, 534, 75

Muñoz-Darias T., et al., 2017, MNRAS, 465, L124

Narayan R., Yi I., 1995, ApJ, 452, 710

Natalucci L., Fiocchi M., Bazzano A., Ubertini P., Roques J.-P., Jourdain E., 2015, ApJ, 813, L21

Negoro H., et al., 2015, The Astronomer's Telegram, 7646

Oda H., Machida M., Nakamura K. E., Matsumoto R., 2007, PASJ, 59, 457

Pelt J., Hoff W., Kayser R., Refsdal S., Schramm T., 1994, A&A, 286, 775

Piano G., Munar-Adrover P., Verrecchia F., Tavani M., Trushkin S. A., 2017, ApJ, 839, 84

Radhika D., Nandi A., Agrawal V. K., Mandal S., 2016, MNRAS, 462, 1834

Remillard R. A., McClintock J. E., 2006, ARA&A, 44, 49

Rodriguez J., et al., 2015, A&A, 581, L9

Roques J. P., Jourdain E., 2016, preprint, (arXiv:1601.05289)

Russell D. M., Fender R. P., Hynes R. I., Brocksopp C., Homan J., Jonker P. G., Buxton M. M., 2006, MNRAS, 371, 1334

Sanchez-Fernandez C., Kajava J. J. E., Motta S. E., Kuulkers E., 2017, A&A, 602, 40

Sano T., Inutsuka S.-i., Miyama S. M., 1998, ApJ, 506, L57

Segreto A., Del Santo M., D'Aí A., La Parola V., Cusumano G., Mineo T., Malzac J., 2015, The Astronomer's Telegram, 7755

Shahbaz T., Ringwald F. A., Bunn J. C., Naylor T., Charles P. A., Casares J., 1994, MNRAS, 271, L10

Shahbaz T., Russell D. M., Covino S., Mooley K., Fender R. P., Rumsey C., 2016, MNRAS, 463, 1822

Shakura N. I., Sunyaev R. A., 1973, A&A, 24, 337

Siebert T., et al., 2016, Nature, 531, 341

Tak H., Mandel K., van Dyk D. A., Kashyap V. L., Meng X.-L., Siemiginowska A., 2016a, preprint, (arXiv:1602.01462)

Tak H., Meng X.-L., van Dyk D. A., 2016b, preprint, (arXiv:1601.05633)

Tanaka Y., Shibasaki N., 1996, ARA&A, 34, 607

Tanaka Y. T., et al., 2016, ApJ, 823, 35

Tetarenko A., Sivakoff G. R., Young K., Wouterloot J. G. A., Miller-Jones J. C., 2015, The Astronomer's Telegram, 7708

Tierney L., 1994, The Annals of Statistics, 22, 1701

Uemura M., et al., 2002, PASJ, 54, L79

Uemura M., et al., 2004, PASJ, 56, S61

Veledina A., Poutanen J., Vurm I., 2011, ApJ, 737, L17

Wagner R. M., Starrfield S. G., Cassatella A., Hurst G. M., Mobberley M., Marsden B. G., 1989, IAU Circ., 4783

Wagner R. M., Bertram R., Starrfield S. G., Howell S. B., Kreidl T. J., Bus S. J., Cassatella A., Fried R., 1991, ApJ, 378, 293

Wagner R. M., Kreidl T. J., Howell S. B., Starrfield S. G., 1992, ApJ, 401, L97

Walton D. J., et al., 2017, ApJ, 839, 110

Yuan F., Zdziarski A. A., Xue Y., Wu X.-B., 2007, ApJ, 659, 541

Życki P. T., Done C., Smith D. A., 1999, MNRAS, 309, 561

van Paradijs J., McClintock J. E., 1994, A&A, 290, 133

van der Laan H., 1966, Nature, 211, 1131

**Table S1.** List of Instruments used for the photometry of the 2015 December outburst in V404 Cyg.

CODE*	Telescope (& CCD)	Observatory (or Observer)	Site
COO	T07 <sup>†</sup> 43cm+STL-1100M	AstroCamp Observatory	Nerpio, Spain
	T21 <sup>†</sup> 43cm+FLI-PL6303E	iTelescope.Net Mayhill	New Mexico, USA
	T11 <sup>†</sup> 50cm+FLI ProLine PL11002M	iTelescope.Net Mayhill	New Mexico, USA
CRI	38cm K-380+Apogee E47	Crimean astrophysical observatory	Crimea
deM	29cm SC+QSI-516wsg	Observatorio Astronomico del CIECEM	Huelva, Spain
DPV	28cmSC+MII G2-1600	Astronomical Obs. on Kolonica Saddle	Slovakia
	35cmSC+MII G2-1600	Astronomical Obs. on Kolonica Saddle	Slovakia
	VNT 1m+FLI PL1001E	Astronomical Obs. on Kolonica Saddle	Slovakia
GFB	CDK 50cm+Apogee U6	William Goff	California, USA
Ioh	30cmSC+ST-9XE CCD	Hiroshi Itoh	Tokyo, Japan
Kai	28cm SC+ST7XME	Kiyoshi Kasai	Switzerland
Kis	25cm SC+Alta F47	Seiichiro Kiyota	Kamagaya, Japan
KU2	40cm SC+Alta U6	Kyoto U. Team	Kyoto, Japan
Mdy	35cm SC+ST10XME	Yutaka Maeda	Nagasaki, Japan
OKU	51cm+Andor DW936N-BV	OKU Astronomical Observatory	Osaka, Japan
Sac	20cmL+ST-7XMEi	Atsushi Miyashita	Tokyo, Japan
SWI	C14 35cmSC+ST10XME	William L. Stein	New Mexico, USA
Trt	25cm ALCCD5.2 (QHY6)	Tamás Tordai	Budapest, Hungary
PXR	FTN 2.0m+E2V 42-40	LCOGT <sup>‡</sup>	Hawaii, USA
	35cmSC+SXV-H9 CCD	Roger D. Pickard	UK

\*Observer's code: COO (Lewis M. Cook), CRI (Crimean Observatory), deM (Enrique de Miguel), DPV (Pavol A. Dubovsky), GFB (William Goff), Ioh (Hiroshi Itoh), Kai (Kiyoshi Kasai), Kis (Seiichiro Kiyota), KU2 (Kyoto Univ. team), Mdy (Yutaka Maeda), OKU (Osaka Kyoiku Univ. team), Sac (Atsushi Miyashita), SWI (William L. Stein), Trt (Tamás Tordai), PXR (Roger D. Pickard).

<sup>†</sup>itelescope.net.

<sup>‡</sup>Las Cumbres Observatory Global Telescope Network.

## APPENDIX A: DETAILS OF THE BAYESIAN MODEL, IMPLEMENTATION, AND MODEL CHECKING

We use a Bayesian model (Tak et al. 2016a) to estimate the time lag between optical and X-ray light curves. The notation  $\mathbf{x} = (x_1, \dots, x_n)$  indicates the observed magnitudes of the X-ray light curve whose reported standard deviations of the measurement errors are  $\boldsymbol{\delta} = (\delta_1, \dots, \delta_n)$  at  $n$  observation times  $\mathbf{t}_x = (t_{x_1}, \dots, t_{x_n})$ . Similarly, the observed magnitudes of the optical light curve are  $\mathbf{y} = (y_1, \dots, y_m)$  with reported standard deviations of the measurement errors  $\boldsymbol{\eta} = (\eta_1, \dots, \eta_m)$  at  $m$  observation times  $\mathbf{t}_y = (t_{y_1}, \dots, t_{y_m})$ . The number of observations for the X-ray light curve  $n$  can be different from that for the optical light curve  $m$  and the observation times of the X-ray light curve  $\mathbf{t}_x$  can be different from those of the optical light curve  $\mathbf{t}_y$ . The model assumes that the observed magnitudes are generated from Gaussian distributions centred at the latent magnitudes with standard deviations of the measurement errors, i.e.,

$$x_i \mid X(t_{x_i}) \sim N\left(X(t_{x_i}), \delta_i^2\right) \text{ for } i = 1, 2, \dots, n, \quad (\text{A1})$$

$$y_j \mid Y(t_{y_j}) \sim N\left(Y(t_{y_j}), \eta_j^2\right) \text{ for } j = 1, 2, \dots, m, \quad (\text{A2})$$

where  $X(t_{x_i})$  and  $Y(t_{y_j})$  are the latent magnitudes of the X-ray and optical light curves at times  $t_{x_i}$  and  $t_{y_j}$ , respectively. A curve-shifted model (Pelt et al. 1994) assumes that the latent optical light curve is a shifted version of the latent X-ray light curve, i.e.,

$$Y(t_{y_j}) = X(t_{y_j} - \Delta) + \beta_0, \quad (\text{A3})$$

where  $\Delta$  is the time delay in days and  $\beta_0$  is the magnitude offset between the latent optical and X-ray light curves. Us-

ing (A3), we re-express (A2) as, for  $j = 1, 2, \dots, m$ ,

$$y_j \mid X(t_{y_j} - \Delta), \Delta, \beta_0 \sim N\left(X(t_{y_j} - \Delta) + \beta_0, \eta_j^2\right). \quad (\text{A4})$$

We assume that the latent light curve follows a continuous-time damped random walk (DRW) process (Kelly et al. 2009) whose stochastic differential equation is defined as

$$dX(t) = -\frac{1}{\tau}(X(t) - \mu)dt + \sigma dB(t),$$

where  $\mu$  and  $\sigma$  denote the overall mean and short-term variation of the DRW process on the magnitude scale, respectively,  $\tau$  is a timescale of the process in days, and  $B(t)$  is a standard Brownian motion. The solution of this stochastic differential equation leads to the Gaussian distributions of the latent magnitudes as follows. We use the notation  $\mathbf{t}^\Delta = (t_1^\Delta, \dots, t_{n+m}^\Delta)$  to denote the sorted vector of  $n + m$  observation times among the  $n$  observation times  $\mathbf{t}_x$  and the  $m$  time-delay-shifted observation times  $\mathbf{t}_y - \Delta$ . Then,

$$\begin{aligned} X(t_1^\Delta) &\sim N\left(\mu, \frac{\tau\sigma^2}{2}\right), \text{ and for } j = 2, 3, \dots, n+m, \\ X(t_j^\Delta) \mid X(t_{j-1}^\Delta) &\sim N\left(\mu + a_j(X(t_{j-1}^\Delta) - \mu), \frac{\tau\sigma^2}{2}(1 - a_j^2)\right), \end{aligned} \quad (\text{A5})$$

where  $a_j = \exp(-(t_j^\Delta - t_{j-1}^\Delta)/\tau)$  and we suppress conditioning on  $\Delta$ ,  $\mu$ ,  $\sigma$ , and  $\tau$  in (A5).

Our independent and jointly proper prior distributions

**Table S2.** Log of observations of the outburst of V404 Cyg from December, 2015 to January, 2016.

Start*	End*	Mag <sup>†</sup>	Error <sup>‡</sup>	N <sup>§</sup>	Obs <sup>  </sup>	Band <sup>#</sup>	exp[s] <sup>¶</sup>
80.5857	80.6428	16.471	0.010	67	GFB	<i>CV</i>	60
81.5472	81.5759	14.871	0.029	17	Kis	<i>I<sub>C</sub></i>	60
81.5840	81.6288	14.908	0.055	19	COO	<i>I<sub>C</sub></i>	120
82.1913	82.3047	14.762	0.016	97	Kai	<i>I<sub>C</sub></i>	30
82.2616	82.3117	16.270	0.015	58	deM	<i>CV</i>	60
82.5703	82.5799	14.720	0.038	5	FJQ	<i>I<sub>C</sub></i>	60
82.8506	82.8902	14.677	0.033	72	Sac	<i>I<sub>C</sub></i>	90
82.8654	82.9298	14.469	0.016	76	Ioh	<i>I<sub>C</sub></i>	60
83.2243	83.3247	14.641	0.017	96	Kai	<i>I<sub>C</sub></i>	30
83.8717	83.9765	14.666	0.018	113	Ioh	<i>I<sub>C</sub></i>	60
83.9423	83.9762	2.092	0.023	54	KU2	<i>CV</i>	30
84.1944	84.3028	14.438	0.029	121	Kai	<i>I<sub>C</sub></i>	30
84.8845	84.9610	1.778	0.008	194	KU2	<i>CV</i>	30
84.8949	84.9487	14.536	0.016	58	Ioh	<i>I<sub>C</sub></i>	60
85.1498	85.2349	17.141	0.101	14	CRI	<i>V</i>	540
85.1520	85.2370	15.580	0.091	14	CRI	<i>R<sub>C</sub></i>	540
85.1541	85.2327	14.455	0.082	13	CRI	<i>I<sub>C</sub></i>	540
85.8582	85.9476	1.474	0.013	225	KU2	<i>CV</i>	30
85.8590	85.8949	14.469	0.036	46	Kis	<i>I<sub>C</sub></i>	60
85.8742	85.9006	14.204	0.029	45	Sac	<i>I<sub>C</sub></i>	90
85.8807	85.9853	14.177	0.027	61	Ioh	<i>I<sub>C</sub></i>	60
85.8896	85.9168	14.440	0.026	25	OKU	<i>I<sub>C</sub></i>	90
86.1662	86.2920	13.832	0.032	170	DPV	<i>I<sub>C</sub></i>	60
86.2803	86.3182	14.721	0.017	44	deM	<i>I<sub>C</sub></i>	60
86.5761	86.5853	14.761	0.022	8	FJQ	<i>I<sub>C</sub></i>	60
86.5864	86.6248	15.484	0.017	48	GFB	<i>R<sub>C</sub></i>	60
86.8507	86.8922	14.088	0.064	87	Kis	<i>I<sub>C</sub></i>	60
86.8620	86.9545	14.479	0.032	155	OKU	<i>I<sub>C</sub></i>	90
87.1656	87.2502	15.685	0.042	165	Trt	<i>CV</i>	30
87.1920	87.2546	13.993	0.084	52	Kai	<i>I<sub>C</sub></i>	30
87.5755	87.6155	16.053	0.013	50	GFB	<i>R<sub>C</sub></i>	60
87.8738	87.9768	13.161	0.027	141	Ioh	<i>I<sub>C</sub></i>	60
87.8743	87.9645	0.332	0.023	206	KU2	<i>CV</i>	30
88.1771	88.2466	14.972	0.075	97	Trt	<i>V</i>	30
88.2894	88.3206	13.840	0.058	44	PXR	<i>I<sub>C</sub></i>	60
88.5759	88.6195	14.942	0.045	50	GFB	<i>R<sub>C</sub></i>	60
88.8485	88.8857	13.585	0.055	70	Kis	<i>I<sub>C</sub></i>	60
88.8652	88.9784	13.321	0.024	229	Ioh	<i>I<sub>C</sub></i>	60
89.5859	89.6227	16.246	0.011	46	GFB	<i>R<sub>C</sub></i>	60
89.8472	89.8826	14.856	0.032	46	Kis	<i>I<sub>C</sub></i>	60
89.9381	89.9754	13.794	0.020	79	Ioh	<i>I<sub>C</sub></i>	60
89.9390	89.9591	0.822	0.031	42	KU2	<i>CV</i>	30
90.8639	90.9495	14.549	0.020	60	Ioh	<i>I<sub>C</sub></i>	60
90.8702	90.9571	1.711	0.022	115	KU2	<i>CV</i>	30
90.8989	90.9337	15.957	0.026	45	Mdy	<i>R<sub>C</sub></i>	30
91.1727	91.2256	17.334	0.049	75	Trt	<i>CV</i>	60
91.5676	91.6260	12.413	0.079	154	SWI	<i>I<sub>C</sub></i>	15
91.8560	91.9038	15.126	0.044	40	Sac	<i>I<sub>C</sub></i>	90
94.9056	94.9321	2.204	0.031	22	KU2	<i>CV</i>	30
95.2544	95.2997	14.948	0.019	24	PXR	<i>I<sub>C</sub></i>	60
97.8620	97.8926	14.909	0.028	28	Ioh	<i>I<sub>C</sub></i>	60

<sup>\*</sup>BJD – 2457300.0.

<sup>†</sup>Mean magnitude.

<sup>‡</sup>1 $\sigma$  of mean magnitude.

<sup>§</sup>Number of observations.

<sup>||</sup>see the annotation in Table S1 and FJQ (Foster James)

<sup>#</sup>Filter. “*I<sub>C</sub>*”, “*R<sub>C</sub>*”, “*V*” and “*CV*” mean *I<sub>C</sub>*, *R<sub>C</sub>*, *V* and no (clear) filter.

**Table S3.** Comparison stars in the photometric campaign of the 2015 December outburst in V404 Cyg.

Observer*	Comparison star	RA (J2000)	Dec (J2000)
COO	AUID 000-BCL-455	20:23:53.43	+33:52:24.6
CRI	USNO1238.0435621	20:24:07.16	+33:50:51.8
deM	AUID 000-BCL-468	20:24:08.89	+33:54:38.6
DPV	UCAC4 620-101865	20:24:07.18	+33:50:51.7
GFB	AUID 000-BCL-475	20:24:26.08	+33:49:51.4
Ioh, Kai	AUID 000-BCL-460	20:23:56.47	+33:48:16.9
Mdy, Kis, Sac	AUID 000-BCL-467	20:24:07.24	+33:50:52.2
KU2	USNO1200.15285418	20:24:18.72	+33:53:13.9
OKU, Sac	AUID 000-BCL-476	20:24:28.31	+33:51:13.5
SWI	AUID 000-BCL-471	20:24:59.41	+33:57:56.6
Trt	AUID 000-BCL-472	20:24:18.66	+33:53:12.6
PXR	AUID 000-BCL-458	20:23:55.26	+33:51:14.8

\* see the annotation in Table S1.

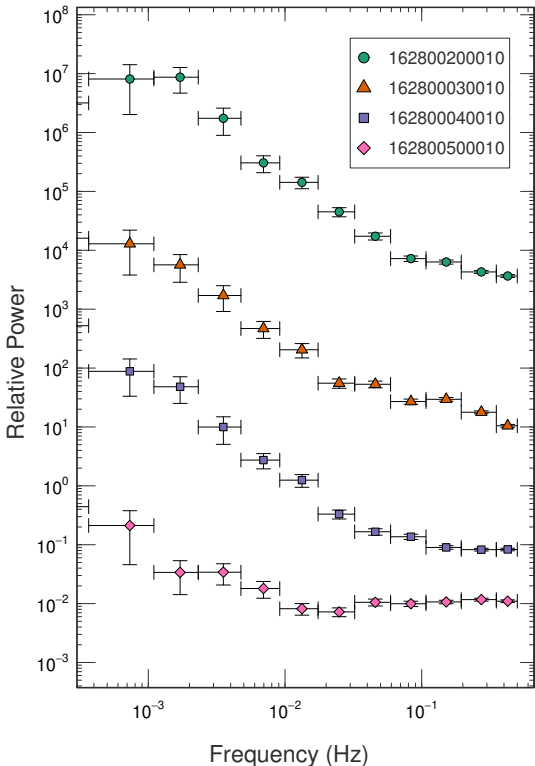


**Figure S1.** PSDs of the X-ray light curves in the SCWs including interval (1) during the day 8.18–8.22 and interval (2) during the day 8.246–8.292. The horizontal and vertical axes represent frequency and power in logarithmic scales. For visibility, the powers in 162800020010, 162800030010, 162800040010 and 162800050010 are offset vertically by the value of  $10^3$ ,  $0$ ,  $10^{-2}$  and  $10^{-5}$ , respectively. The errors of PSDs represent  $\pm 1\sigma$ .

on the model parameters, i.e.,  $\Delta$ ,  $\beta_0$ ,  $\mu$ ,  $\sigma^2$ , and  $\tau$ , are

$$\begin{aligned} \Delta &\sim \text{Uniform}(w_1, w_2) \\ \beta_0 &\sim N(0, 10^5) \\ \mu &\sim \text{Uniform}(-30, 30) \\ \sigma^2 &\sim \text{inverse Gamma}(1, 1) \\ \tau^2 &\sim \text{inverse Gamma}(1, 2 \times 10^{-7}), \end{aligned} \quad (\text{A6})$$

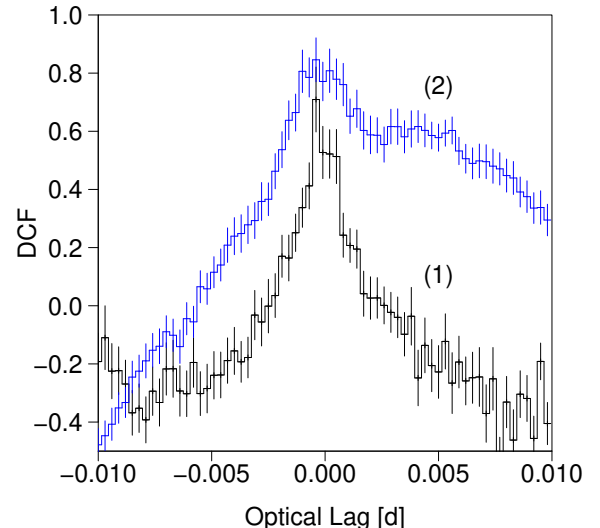


**Figure S2.** Estimated LNDCFs in interval (1) during the day 8.18–8.22 (black lines) and interval (2) during the day 8.246–8.292 (blue lines). The minus and plus signs in the horizontal axis indicate that X-ray emission is delayed to optical emission and that optical emission is delayed to X-ray emission. We can see correlated positive peaks at the  $-35^{+13}_{-13}$  s optical lags in the DCFs as for both two intervals.

where we fix the range of the Uniform distribution of  $\Delta$  at  $(-0.04, 0.04)$  for interval (1) and at  $(-0.046, 0.046)$  for interval (2) to prevent spurious modes of the time delay on the margins of its space and to consider the longer observation period of interval (2). We choose the shape and scale parameters of the inverse Gamma distributions of  $\tau$  and  $\sigma^2$  in a way to constrain  $\Delta$ , considering shorter timescale of the observed data than gravitationally lensed light curves. Further details of the motivation for the choice of prior distributions are given in Sections 2.5 of [Tak et al. \(2016a\)](#).

Our full posterior density,  $\pi(X(t^\Delta), \Delta, \beta_0, \mu, \sigma^2, \tau | \mathbf{x}, \mathbf{y})$ , is proportional to the multiplication of the probability density functions, whose distributions are specified in (A1), (A4), (A5), and (A6). We use a Metropolis-Hastings within Gibbs sampler ([Tierney 1994](#)) to sample the full posterior distribution of the model parameters; see Section 3 of [Tak et al.](#)

(2016a) for details of this sampler. To improve the convergence of the MCMC for  $\Delta$  in the presence of multimodality, we adopt a repelling-attracting Metropolis algorithm (Tak et al. 2016b).

Before implementing the Bayesian method, we first checked the multi-modal behavior of  $\Delta$  by quickly mapping a wide range of  $\Delta$  between  $-86.40$  s and  $86.40$  s using the profile likelihood function of  $\Delta$  defined as

$$L_{\text{prof}}(\Delta) = \max_{\beta_0, \mu, \sigma^2, \tau} L(\Delta, \beta_0, \mu, \sigma^2, \tau).$$

This profile likelihood is proven to be a simple approximation to its marginal posterior distribution; see Section 4 of Tak et al. (2016a). We confirmed that the highest mode is near  $-45$  s and three weak modes are near  $-50$  s and  $-30$  s, and  $-25$  s; the relative heights (the ratio of the profile likelihoods) of the modes near  $-50$  s,  $-30$  s and  $-25$  s compared to the mode near  $-45$  s are  $5.7 \times 10^{-3}$ ,  $5.1 \times 10^{-8}$  and  $6.5 \times 10^{-9}$ , respectively. In interval (2), the dominant mode is at around  $-33$  s and an invisibly small mode is near  $-48$  s; the relative height of the mode near  $-48$  s compared to that of the mode near  $-33$  s is  $2.7 \times 10^{-7}$ .

We initialize three Markov chains near the dominating mode for each time interval, running for 150,000 iterations; we discard the first 50,000 as burn-in iterations. The proposal scale of  $\Delta$  (delta.proposal.scale in Table A1) is set to produce the largest acceptance rate while making the Markov chains jump frequently between the modes identified by the profile likelihood. The average acceptance rate of the time lag is 0.216 for interval (1) and 0.186 for interval (2).

We visually checked our estimates, shifting the optical light curves by the posterior medians of  $\Delta$  and  $\beta_0$  in Figure A1; the fitted model matches the fluctuations of the two light curves well. We also conducted a model checking by plotting the posterior sample of the latent curve in grey; the grey areas encompass most of the observed light curves, which shows how well the fitted model predicts the observed data. A sensitivity analysis, though not shown here, exhibits that our inferential results in Table 2 are robust to changing the scale parameters in the inverse Gamma distributions of  $\sigma^2$  and  $\tau$ .

This paper has been typeset from a  $\text{TeX}/\text{L}\text{A}\text{T}\text{E}\text{X}$  file prepared by the author.

**Table A1.** Initial values of the parameters for each of three Markov chains used in the function `bayesian` of the R package `timedelay` for interval (1) during the day 8.18–8.22 and interval (2) during the day 8.246–8.292.

Names of parameters	(1)	(2)
theta.ini ( $\mu, \sigma, \tau$ ) <sup>*</sup>	(5.30, 100, 0.01) (5.30, 10, 0.1) (5.30, 1, 1)	(5.72, 100, 0.01) (5.72, 10, 0.1) (5.72, 1, 1)
delta.ini <sup>†</sup>	-0.0005827546 -0.0005248843 -0.0004670139	-0.0004405093 -0.0003826389 -0.0003247685
delta.uniform.range <sup>‡</sup>	(-0.04, 0.04)	(-0.046, 0.046)
delta.proposal.scale <sup>§</sup>	0.00005	0.00005
tau.proposal.scale <sup>#</sup>	1	1
tau.prior.shape <sup>¶</sup>	1	1
tau.prior.scale <sup>**</sup>	$2/10^7$	$2/10^7$
sigma.prior.shape <sup>††</sup>	1	1
sigma.prior.scale <sup>††</sup>	1	1
adaptive.delta <sup>§§</sup>	FALSE	FALSE
multimodality <sup>##</sup>	TRUE	TRUE
micro <sup>¶¶</sup>	0	0

<sup>\*</sup>Initial values of the DRW parameters. Unit of magnitudes in  $\mu$  and  $\sigma$ . Unit of days in  $\tau$ .

<sup>†</sup>Initial value of the delay time for MCMC used in three Markov chains. Unit of days.

<sup>‡</sup>Range of uniform prior distribution of the time delay  $\Delta$ . Unit of days.

<sup>§</sup>Proposal scale of the Metropolis step for the time delay  $\Delta$ . Unit of days.

<sup>#</sup>Proposal scale of the Metropolis-Hastings step for  $\log(\tau)$ . Units of  $\tau$  are days.

<sup>¶</sup>Shape parameter of Inverse-Gamma hyper-prior distribution for  $\tau$ .

<sup>\*\*</sup>Scale parameter of Inverse-Gamma hyper-prior distribution for  $\tau$ .

<sup>††</sup>Shape parameter of Inverse-Gamma hyper-prior distribution for  $\sigma^2$ .

<sup>††</sup>Scale parameter of Inverse-Gamma hyper-prior distribution for  $\sigma^2$ .

<sup>§§</sup>We do not use the adaptive MCMC for the time delay  $\Delta$  in the presence of multi-modality because the adaptation may occur at a local mode.

<sup>##</sup>We use a repelling-attracting Metropolis algorithm to sample the time delay  $\Delta$ .

<sup>¶¶</sup>The order of a polynomial regression model. We do not consider the effect of microlensing in the case of V404 Cyg.

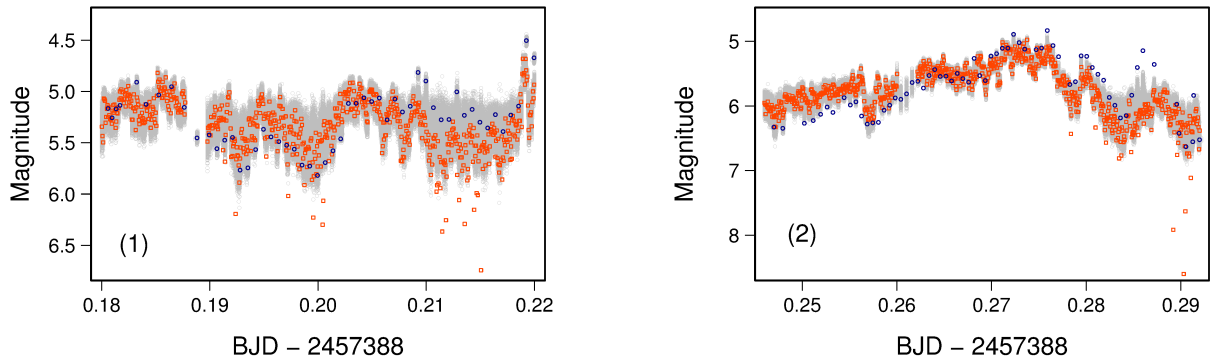


**Figure A1.** The X-ray light curves are denoted by orange squares, the optical light curves are denoted by blue circles, and the posterior samples of latent light curves at intervals of 300 iterations are denoted by grey circles in interval (1) on the day 8.18–8.22 (the left panel) and interval (2) on the day 8.246–8.292 (the right panel). Each optical light curve is shifted by the posterior mode of the time lag in the horizontal axis and by that of the magnitude offset in the vertical axis. The fitted model makes a good match of the fluctuations of the two light curves. The grey areas are encompassing most of the light curves, meaning that the fitted model describes the observed data well.